Original Paper

Determination of the rheological properties of high-viscous glass melts by the cylinder compression method

Rolf Brückner, Yuanzheng Yue and Andreas Habeck

Institut für Nichtmetallische Werkstoffe – Anorganische Werkstoffe –, Technische Universität Berlin, Berlin (Germany)

A detailed description of the cylinder compression method and its application on the viscoelastic behaviour of glass melts is given with the help of closed solutions and equations in contrast to algorithmic methods, like e.g. the finite element method. Special attention is paid to the system deformation and system deformation rate of the testing equipment and to the dissipation of mechanical energy within the specimen and the heat flow from the specimen. The limits of this treatment are discussed with respect to the applicability of the theoretical basis (Gent and Nadai equation) and with respect to the experimental determination of the rheological properties of glass melts. On this basis the pure non-Newtonian viscosity, η_{nN}, can be determined. If very small differences have to be ascertained in the rheological behaviour of glass melts due to small differences in composition or in melting history (e.g. redox condition or bad/good workability), the same conditions concerning the mechanical and thermal equipment and even the same geometry of the glass specimens have to be strictly maintained. Comparison between different glass melts should be made rather on the basis of equal (Newtonian) equilibrium viscosity, η_0, (isochomal conditions) and not on equal temperature. Owing to large thermal effects, the slope of the viscosity-temperature curve at η_0 plays a certain role, particularly for the forming process.

Bestimmung der rheologischen Eigenschaften hochviskoser Glasschmelzen mit der Zylinderstauchmethode

Es wird eine ausführliche Beschreibung der Zylinderstauchmethode und ihrer Anwendung auf das viskoelastische Verhalten von Glasschmelzen mit Hilfe geschlossener Lösungen und Gleichungen gegeben im Gegensatz zu algorithmischen Methoden, wie z.B. der Methode der finiten Elemente. Besondere Aufmerksamkeit wird auf die Systemdeformation und -deformationsgeschwindigkeit der Apparatur und auf die durch Dissipation der mechanischen Energie erzeugte Wärme in der Probe sowie auf die Abgabe der Wärme von der Probe gelegt. Die Grenzen dieser Methode werden im Hinblick auf die Anwendbarkeit der theoretischen Grundlagen (Gent- und Nadai-Gleichung) und im Hinblick auf die experimentelle Bestimmung der rheologischen Eigenschaften der Glasschmelzen diskutiert. Auf dieser Basis kann die reine nicht-Newtonsche Viskosität, η_{nN}, ermittelt werden. Wenn sehr kleine Unterschiede im rheologischen Verhalten von Glasschmelzen aufgrund kleiner Unterschiede in der Zusammensetzung oder Schmelzvergangenheit (z.B. Redoxbedingungen oder schlechte/gute Verarbeitbarkeit) ermittelt werden sollen, müssen die gleichen Bedingungen bezüglich der mechanischen und thermischen Ausrüstung und sogar die gleiche Geometrie der Glasproben strikt eingehalten werden. Vergleiche zwischen verschiedenen Glasschmelzen sollten tunlichst auf der Basis gleicher (Newtonscher) Gleichgewichtsviskositäten, η_0, (isochome Bedingungen) und nicht auf der Basis gleicher Temperaturen gezogen werden. Im Hinblick auf große thermische Effekte spielt der Gradient der Viskositäts-Temperaturkurve, $d\eta_0/dT$, bei η_0, besonders für den Formgebungsprozeß, eine wichtige Rolle.

1. Introduction and objective

Among the various rheological methods for measuring the flow properties of high-viscosity glass melts the rod elongation method was applied [1 to 5] in order to get Newtonian and non-Newtonian flow behaviour up to high tensile loads. Also rotation viscometers can be applied as was done up to extremely high shear rates with the help of a cone/plate viscometer at low viscosities [3]. The advantage of these methods is that pure tensile respectively shear flow is realized over the whole cross-section of the specimen. The disadvantage is that only Newtonian and non-Newtonian viscosities can be determined. In contrast to these methods the parallel-plate plastometer, which was originally applied to determine Newtonian viscosities [6 to 8], was used to determine also non-Newtonian viscosities [3, 4, 9 and 10]. The method was later extended to realize other rheological properties from stress-strain curves of cylindrical glass samples, such as the viscoelastic response, i.e. the relaxation modulus and the first crack due to the limit of the tensile stress component [11 and 12].

Despite of the fact that the stress and strain distributions are somewhat more complicated than in pure tensile and shear experiments, there are three great advantages for the compression experiments; first, the compressive strength of glasses is about one order of magnitude larger than the tensile strength, thus, the measurements and properties can be extended up to about one order of magnitude larger values than those of the tensile experiments; second, the compression method allows the determination of the relaxation modulus and high-temperature tensile strength additionally to the Newtonian/non-Newtonian viscosity; third, the most frequent glass forming processes in practice with very large deformation rates are those which are

---

Received November 11, 1993, revised manuscript January 27, 1994.

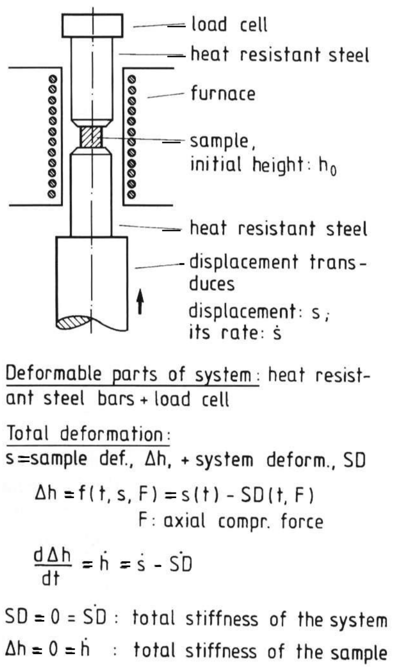

Figure 1. Apparatus (schematic) of the cylinder compression method.

connected to compressive deformations. Therefore, it may be expected that this method appears to be the closest one to industrial applications and practical problems.

The purpose of this paper is to give details about the method of the cylinder compression with respect to the mechanical corrections due to the system deformation and system deformation rate, with respect to the thermal corrections due to the heat dissipated from the mechanical energy within the sample and its heat flow from the sample and to point out the limits of this method.

The glass cylinders can be compressed by a servohydraulic test machine MTS (Material Test System) with very low and high speeds of the working piston (from 0.01 µm/s up to 2 m/s unloaded and up to 20 cm/s under load). The values of the MTS machine force, deformation and deformation rate were collected by a rapid transient recorder (Kontron, München (Germany)) and evaluated by a computer programme. The transient recorder is a four-channel transiscope which has a 12 bit analog-digital transformer with a maximum digital sampling rate of $25 \cdot 10^4$ signals/s at a store depth of 8 kbyte per channel. If no other indications are given, the here applied glass has the composition (in mol%): $74SiO_2$, $16Na_2O$, $10CaO$. The glass samples must have very plane-parallel face areas and the same geometry for very exact comparison.

2. Theoretical basis

The principle of the compression method for glass cylinders may be seen from figure 1. The independent variables are the piston movement, *s*, versus time, *t*, i.e. the constant piston velocity, $\dot{s}$, (diagrams no. 1 and 2 in figure 2). The response is the force, *F*, measured by the force cell, resulting in one of the curves of diagram no. 3 (figure 2) which has to be registered by a fast transient recorder. Now, the first two corrections of the data of

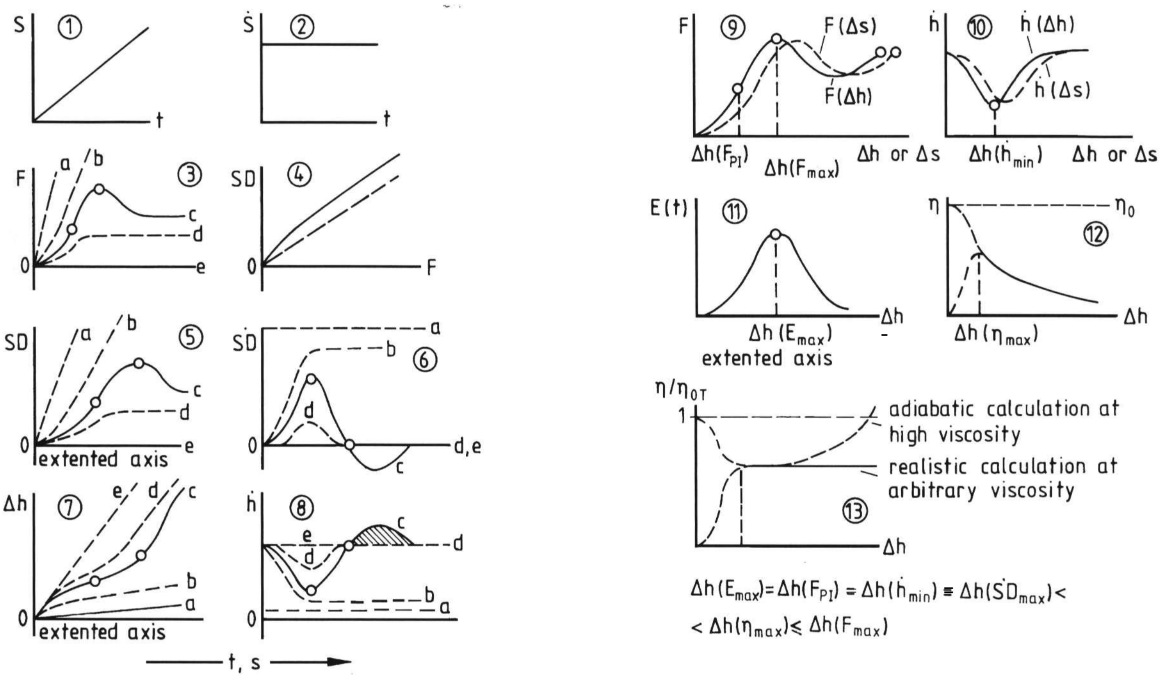

Figure 2. Stepwise procedure and information on the viscoelastic response of glass samples and the elastic response of the coupled parts of the experimental equipment. Diagrams no. 1 to 13 with a = sample and system ideal elastic; b = sample ideal elastic, system real (delayed) elastic; c = sample with high stiffness, system real elastic; d = sample with low stiffness, system real elastic, e = sample totally plastic.

this curve have to be made, the deformation of the apparatus system or the system deformation, SD, and the system deformation rate, $S\dot{D} = \mathrm{d}(SD)/\mathrm{d}t$, with respect to the correct deformation rate of the sample. Thus, the real sample deformation is $\Delta h = s - SD$ and the real deformation rate of the sample is $\mathrm{d}h/\mathrm{d}t = \dot{h} = |\Delta\dot{h}| = \dot{s} - \dot{S}D$. SD can be determined experimentally from experiments with an incompressible corundum plate instead of the glass sample at various temperatures (diagram no. 4 in figure 2) and may be represented by the correction function

$$SD = aF(t) + b - b/(10^{n \cdot F(t)}) \tag{1}$$

with $n = 0.04$, in which a, b and n are constants which are only slightly temperature-dependent within the range of experiments due to the good quality of the steel bars. From the diagrams no. 3 and 4 the diagrams no. 5 to 8 follow step by step with the help of a computer programme. From the diagrams no. 7 and 8, the real sample deformation, Δh, and deformation rate, $\dot{h}$, follow as is demonstrated in the corrected diagrams no. 9 and 10 in figure 2 which are based on the sample deformation, Δh. From diagram no. 9 the time-dependent maximum elastic modulus (relaxation modulus) is determined by

$$E(t)_{\max} = \frac{h_0}{A}\left(\frac{\mathrm{d}F}{\mathrm{d}\Delta h}\right)_{\mathrm{PI}} = \frac{h_0}{A}\left(\frac{\dot{F}}{\dot{h}}\right)_{\mathrm{PI}} = E(t)_{\mathrm{PI}} \tag{2}$$

where A is the cross-section of the cylindrical glass sample, h_0 the initial height, $\dot{F} = \mathrm{d}F/\mathrm{d}t$ and $\dot{h} = |\mathrm{d}h/\mathrm{d}t|$ at the point of inflexion (PI) of the $F(\Delta h)$ curve and at $E(t)_{\max}$, respectively.

The viscosity as a function of Δh is determined by the Gent equation [6], which is valid for non-slip condition at the face area of the glass cylinder:

$$\eta(t) = F[3V\dot{h}(V/(2\pi h(t)^5) + 1/h(t)^2)]^{-1} \tag{3}$$

where V is the volume of the sample. $\eta(t)$ is transformed into $\eta(\Delta h)$ (diagram no. 12 in figure 2) by means of diagram no. 7. The lower dashed part of the curve is unrealistic up to the maximum but from there on it is realistic. The estimated upper dashed and dotted part of the curve characterizes the break-down of the Newtonian flow, between $\Delta h = 0$ to $\Delta h(\eta_{\max})$ if the deformation rate, $\dot{h}$, is large enough to induce non-Newtonian flow behaviour. During the short interval between $\Delta h = 0$ and $\Delta h(\eta_{\max})$ the dissipated mechanical energy is still very low, thus, no relevant temperature increase takes place and the ratio η/η_0 depends only on the deformation rate $\dot{h}$ and on axial stress, σ, respectively, at a given Δh value (diagram no. 13 in figure 2). At larger deformations, Δh, however, the dissipated energy will be heating up the sample and will change the Newtonian viscosity, η_0, to η_{0T}. The maximum temperature increase which produces this change will be due to the adiabatically dissipated heat, Q_{in}:

$$\Delta T_{\max} = \frac{Q_{\mathrm{in}}}{c_{\mathrm{p}} \cdot M} = \frac{1}{c_{\mathrm{p}} \cdot M}\int_0^{\Delta h} F \cdot \mathrm{d}\Delta h \tag{4}$$

where c_{p} is the specific heat and M is the mass of the sample.

Therefore, the dissipated heat Q_{in} does not remain constant but increases with Δh and $\dot{h}$. A more detailed analysis takes into account not only the heat of dissipation produced within the sample, Q_{in}, but also the heat loss of the sample caused by conduction, radiation and convection flow, Q_{out}, [19]:

$$Q_{\mathrm{out}} = (\alpha_{\mathrm{cd}}\, 2A_{\mathrm{cd}} + \alpha_{\mathrm{r}} A_{\mathrm{r}} + \alpha_{\mathrm{cv}} A_{\mathrm{r}})\Delta t\, \Delta T_{\mathrm{net}} \tag{5}$$

where α_{cd} is the heat conduction coefficient, α_{r} the heat radiation coefficient and α_{cv} the heat convection coefficient, $A_{\mathrm{cv}} = A_{\mathrm{r}}$, A_{cd} and A_{r} the corresponding areas, $\Delta t = \Delta h/\dot{h}$ the duration of the compression experiment and ΔT_{net} the real (net) temperature increase in the sample produced by the heat quantity, Q_{net}:

$$Q_{\mathrm{net}} = Q_{\mathrm{in}} - Q_{\mathrm{out}} = c_{\mathrm{p}} \cdot M \cdot \Delta T_{\mathrm{net}}$$

or (6)

$$\Delta T_{\mathrm{net}} = Q_{\mathrm{net}}/(c_{\mathrm{p}} M) = (Q_{\mathrm{in}} - Q_{\mathrm{out}})/(c_{\mathrm{p}} M)\,.$$

The calculation is shown in sections 3.2. and 7. The corresponding viscosity decrease has to be regarded by the VFT equation, thus, the Newtonian viscosity, η_0, changes to η_{0T} depending on ΔT_{net} or $\Delta T_{\max}$ by the following equations:

$$\eta_{0T_{\mathrm{net}}} = A + \frac{B}{T + \Delta T_{\mathrm{net}} - T_0}\,,$$

$$\eta_{0T_{\max}} = A + \frac{B}{T + \Delta T_{\max} - T_0}\,, \tag{7}$$

$$\eta_{0T_{\max}} \leq \eta_{0T_{\mathrm{net}}} \leq \eta_0\,.$$

If now the measured (non-Newtonian) viscosity is determined by the Gent equation as $\eta(\dot{h}, \Delta T) = \eta$, the temperature increase may shift η_0 by the value of η_{0T} and the ratio η/η_{0T} represents the real (because temperature-corrected) relative non-Newtonian viscosity. This was done in earlier papers [10 to 12]. From equations (4 to 6) is seen that the net temperature increase ΔT_{net} approaches $\Delta T_{\max}$ as the deformation rate increases by one and the same degree of compression, Δh, because it is $\mathrm{d}Q_{\mathrm{in}} \propto \mathrm{d}\Delta h$ (see equations (4 and 15)), therefore, $\dot{Q}_{\mathrm{in}} = \mathrm{d}Q_{\mathrm{in}}/\mathrm{d}t \propto \dot{h}$ and $\mathrm{d}Q_{\mathrm{out}} \propto \Delta T_{\mathrm{net}}\,\Delta t$ (see equations (5 and 16)), therefore, $\dot{Q}_{\mathrm{out}} = \mathrm{d}Q_{\mathrm{out}}/\mathrm{d}t \propto \Delta T_{\mathrm{net}}$. This means that with increasing $\dot{h}$ the heating rate, $\dot{Q}_{\mathrm{in}}$, in the sample will exceed the cooling rate, $\dot{Q}_{\mathrm{out}}$, and finally $\dot{Q}_{\mathrm{out}}$ can be neglected as compared with $\dot{Q}_{\mathrm{in}}$ if $\dot{h}$ is high enough, i.e.:

$$\dot{Q}_{\mathrm{in}} \gg \dot{Q}_{\mathrm{out}}$$

or (8)

$$\lim_{\Delta t \to 0;\, \dot{h} \to \infty} \Delta T_{\mathrm{net}} = \Delta T_{\max}\,,$$

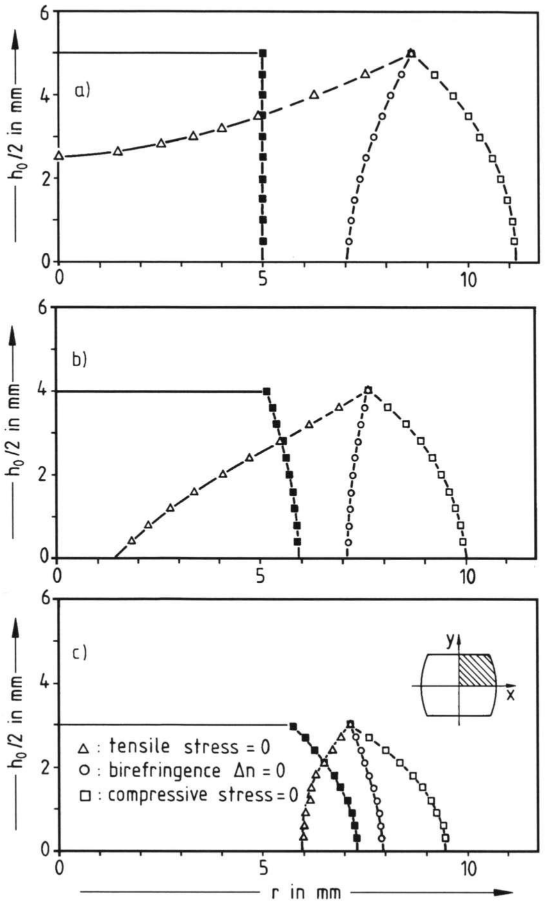

Figures 3a to c. Three steps of cylinder deformation (first quadrant section) $\Delta h/h_0 = 0$, 20 and 40 % and limiting curves for tensile stress $\sigma_t = 0$, birefringence $\Delta n = 0$ ($\sigma_t = \sigma_z$) and compressive stress $\sigma_z = 0$; a) $h/h_0 = 1$, b) $h/h_0 = 0.8$, c) $h/h_0 = 0.6$.

in other words: the compression process becomes more and more adiabatic as $\dot{h}$ increases and this is the case at higher temperatures, i.e. at lower viscosities. On the other hand, if Δt is very large (i.e. $\dot{h}$ is very small), then $\dot{Q}_{\text{in}} \approx \dot{Q}_{\text{out}}$, thus, $\dot{Q}_{\text{net}} \approx 0$ and therefore:

$$\lim_{\Delta T\to\infty;\ \dot{h}\to 0} \Delta T_{\text{net}} = 0$$

if (9)

$$\dot{Q}_{\text{in}} \approx \dot{Q}_{\text{out}} \, .$$

The stress distribution within the compressed glass cylinder is now considered with the help of the Nadai equations [13], which describe the stress distribution in a compressed cylinder with no slip at the face area (the plane circular ends of the specimens). The stress components are (here $h_N = h/2$ in agreement with the original Nadai nomenclature):

radial and tangential stresses:

$$\sigma_r = \sigma_t = 3\eta v_0 (r^2 - R^2 - 4z^2 + 2h_N^2)/(4h_N^3)\,; \qquad (10)$$

axial stress

$$\sigma_z = 3\eta v_0 (r^2 - R^2 + 2z^2 - 4h_N^2)/(4h_N^3) \qquad (11)$$

in which R = radius of the cylinder, r = radial coordinate due to the amount of compression and due to the axial z coordinate, $h_N = h/2$ = half of the cylinder height, η = viscosity and $v_0 = \dot{h}/2$ = axial deformation rate. For a given degree of compression the lines or the planes can be calculated at which tensile and compressive stresses are zero. This leads to the expressions:

tensile stress: $\sigma_t = 0$: $r^2 = R^2 + 4z^2 - 2h_N^2$, (12)

compressive stress: $\sigma_z = 0$: $r^2 = R^2 - 2z^2 + 4h_N^2$. (13)

The first quadrant of the longitudinal cross-section of a compressed cylinder is shown at three different degrees of compression in figures 3a to c. As is shown, the limiting curve for axial compressive stress zero ($\sigma_z = 0$, symbols □) is outside of the cylinder dimensions at compression degrees up to more than 40 %. On the left side of this limiting curve ($\sigma_z = 0$) there are axial compressive stresses. On the other hand, the limiting curve for the tensile stresses ($\sigma_t = 0$, symbols △) is partly outside and partly inside the cylinder dimensions. Thus, on the left side of the curve $\sigma_t = 0$ there are exclusively compressive stresses, on the right side of this curve there are compressive and tensile stresses and on the right side of the curve $\sigma_z = 0$ there are exclusively tensile stresses.

It was shown in a recent paper [14] by means of under load frozen-in birefringence at a viscosity of $\eta_0 = 10^{11}$ Pa s that the Nadai equations agree well with the experiments and with the demonstrated stress distribution. It could also be shown in separated experiments that the calculated alteration of the cylinder geometry with increasing deformation, Δh, agrees also well with the experiment (see section 3.3.) at least up to a deformation of about $\Delta h/h_0 = 30$ %. Such large deformations are applied only in certain experiments when the first crack has to be registered in order to determine the tensile strength of the glass melt and the critical deformation rate, $\dot{h}_c$, respectively, which is that $\dot{h}$ at which the first crack appears at a given deformation, Δh. The other properties, such as non-Newtonian viscosity and relaxation modulus, are usually determined at much smaller degrees of deformation (about 1 to 7 % of h_0). But for practical reasons it might be of special value sometimes to get the non-Newtonian viscosity and to register the first crack also at larger deformations with larger heat effects, where among these effects the slope of the viscosity-temperature curve plays a certain role. But those experiments are only meaningful for more comparative studies than for absolute measurements. In such experiments the volume of all samples has to be kept equal because the heat dissipation and heat loss of the samples have to be comparable. It is also important to compare

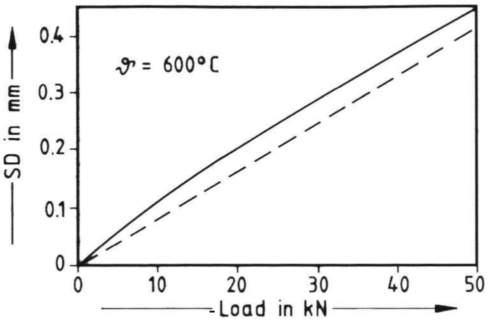

Figure 4. System deformation, *SD*, versus load, $SD = a \cdot F(t) + b - \frac{b}{10^{0.04 \cdot F(t)}}$ with $a = 0.00787$ and $b = 0.055$ at 600 °C and at $\dot{s} = 0.008$ mm/s.

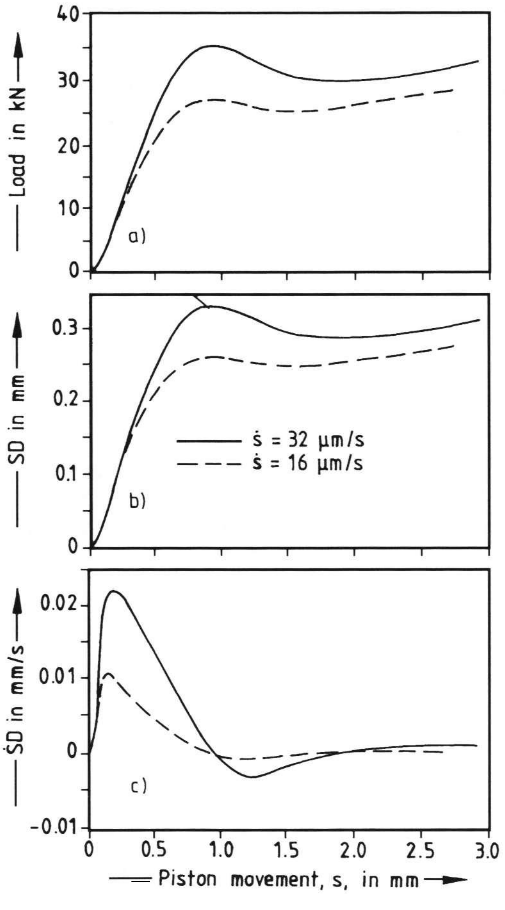

Figures 5a to c. Load, *F* (figure a), system deformation, *SD* (figure b), and system deformation rate, $\dot{SD}$ (figure c), versus piston movement, *s*, at a (Newtonian) equilibrium viscosity $\eta_0 = 10^{11}$ Pa s.

the properties of different samples not at the same temperature but rather at the same (Newtonian) equilibrium viscosities, η_0.

3. Results

3.1. Mechanical influences on the numerical treatment of the cylinder compression experiment

The diagrams no. 1 to 4 in figure 2 are given directly from the experiment (here: schematically). The next step is to determine the constants *a* and *b* of the correction function (1) at various temperatures from the dates of diagram no. 4. With the help of diagram no. 3 the system deformation $SD(t, s)$ and its rate follow (diagrams no. 5 and 6) for which five typical variations can be obtained at and after the point of inflexion (PI): a) characterizes ideal elastic properties of sample and system; b) results from an ideal elastic sample (e.g. corundum cylinder) and a (delayed) real elastic system; c) holds for a glass sample with high stiffness; d) a glass sample with low stiffness and e) characterizes a totally plastic sample. The shadowed area indicates the excess deformation rate produced by the expansion of the system after the compression phase at very high deformation rates. These characteristics are not of absolute meaning because they depend strongly on the deformation rate and, therefore, also on the axial stress as it is usual for viscoelastic behaviour.

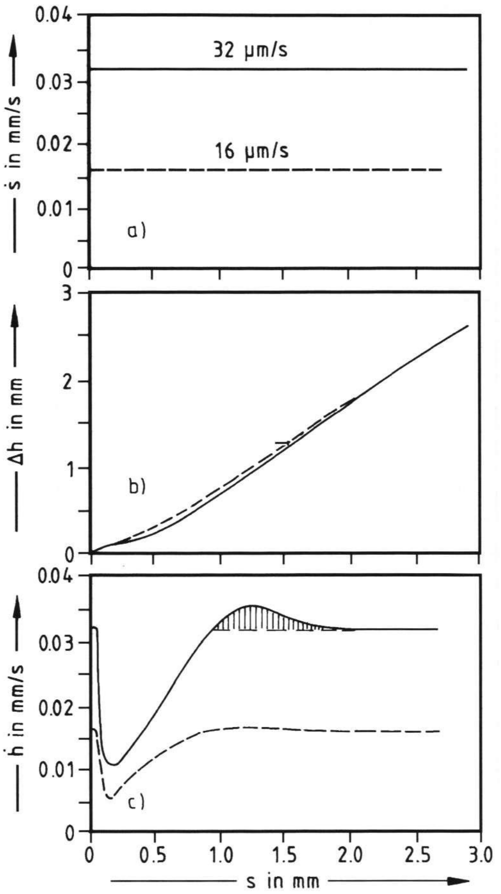

Figures 6a to c. Piston velocities, $\dot{s}$ (figure a), axial compressive deformations of the sample, Δh (figure b), and deformation rates, $\dot{h}$ (figure c), versus piston movement, *s*, at a Newtonian viscosity of $\eta_0 = 10^{11}$ Pa s.

Examples for this part of the procedure are shown in a quantitative way in the case of a silicate glass (see section 1.) in figure 4 where the constants of equation (1) are determined from the system deformation, *SD*, versus load at 600 °C, and in figures 5a to c for two piston velocities: $\dot{s} = 32$ and 16 µm/s. Figure 5a represents the

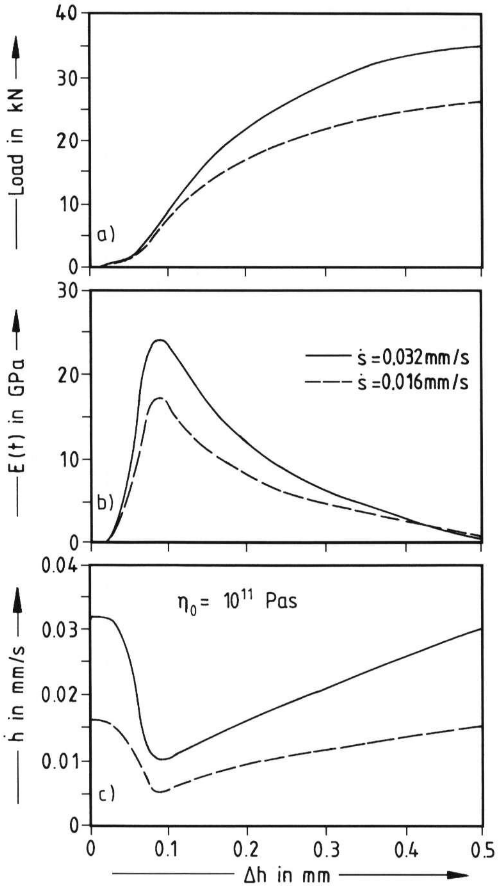

Figures 7a to c. Load, F (figure a), relaxation modulus, $E(t)$ (figure b), and axial deformation rate, $\dot{h}$ (figure c), versus axial deformation, Δh, at $\eta_0 = 10^{11}$ Pa s.

load, figure 5b the system deformation SD and figure 5c the system deformation rate $\dot{SD} = \mathrm{d}SD/\mathrm{d}t$ versus piston movement. Subtraction of $\dot{SD}$ (figure 5c) from the piston velocity $\dot{s}$ (figure 6a) or the first differentiation of the sample deformation Δh (figure 6b) with time leads to the deformation rate, $\dot{h} = \mathrm{d}\Delta h/\mathrm{d}t$, of the sample versus piston movement, s, (figure 6c). The convex part of the $\dot{h}$ versus s diagram in figure 6c indicates that the deformation rate, $\dot{h}$, exceeds the piston velocity, $\dot{s}$. The reason for that is the release of the stored elastic energy of the apparatus which is caused by the combined action of the structure-dependent non-Newtonian flow and of the thermally induced (Newtonian) viscosity decrease due to the dissipation of the mechanical energy (see section 3.2.); and both properties depend on composition and on structure of the glass melt.

From figures 5a to c and 6a to c the diagrams of figures 7a to c are obtained as load-Δh curves (load versus real sample deformation, figure 7a) and as $\dot{h}-\Delta h$ curves (figure 7c), which show extended Δh axes from $\Delta h = 0$ to 0.5 mm. The relaxation modulus, $E(t)$ (figure 7b), can be determined from figure 7a according to equation (2), here as an example at a Newtonian viscosity of 10^{11} Pa s for the standard glass (see section 2.). In a similar manner the curves of figures 8a to f are obtained at two further Newtonian viscosities (10^{10} and 10^{8} Pa s) and for three piston rates for each viscosity. From figures 7a to c and 8a to f is clearly seen that within the initial phase of the viscoelastic range the maximum relaxation modulus $E(t)_{\max}$ is obtained together with a minimum deformation rate, $\dot{h}$, both being important for the relaxation behaviour and for the characterization of the stiffness of a glass melt. Three typical dependencies are the consequence of figures 7a to c and 8a to f: first, $E(t)_{\max}$ increases with increasing $\dot{s}$; second, $E(t)_{\max}$ and $\dot{h}_{\min}$ are shifted to larger values of Δh with increasing piston velocity, $\dot{s}$, and this increases with decreasing (Newtonian) viscosity; third, the ratio $\dot{h}_{\min}/\dot{s}$ becomes smaller with increasing $\dot{s}$.

In figures 9a and b are plotted the load, $F(t)$, and the deformation rate of the sample, $\dot{h}(t)$, versus Δs and $\Delta h = \Delta s - SD$ in order to demonstrate that SD and also $\dot{SD}$ have a large influence on the exact calculation of the results. This means that the correct compression ($\Delta h/h_0$ and $E(t)_{\max}$) values and all properties at all (non-Newtonian flow, tensile strength) can be obtained only from plots $F(t)$ and $\dot{h}(t)$ versus Δh and not versus Δs.

In order to determine quantitatively the tensile strength of a high-viscous cylindrical glass melt during the compression procedure, Nadai's tensile stress equations were applied and further developed by Hessenkemper and Brückner [11]. When equation (3) is introduced into equation (23) of [11] the relation:

$$\sigma(t)_{\text{tensile}} = F(t)\,\frac{2R^2[(h_0/h(t))^{1.5}-1]+h^2(t)}{V[V/(\pi \mathrm{h}^2(t))+2h(t)]} = F(t)\,c(t) \qquad (14)$$

follows where $c(t)$ is the tensile stress factor for the stress at the equatorial line of the compressed cylinder. Within the compression range, $\Delta h/h_0 \approx 0$ to 35 %, $c(t)$ remains practically constant (figures 10a and b). From equation (14) follows that $\sigma(t)_{\text{tensile}}$ depends only on the load, $F(t)$, and on the geometries of the samples at the beginning (h_0, R) and at the end of the experiment ($h(t)$). In combination with the registration of the first crack of the sample [9 to 12] $\sigma(t)_{\text{tensile}}$ is identical with the tensile strength, $\sigma(t)_{\text{tensile}}^{\max}$ (see figures 9a and b to 11).

3.2. Thermal influences on the numerical treatment of the cylinder compression experiment

The considerations now start at a point of the procedure where all relevant properties and parameters are based on and related to Δh, i.e. to the real corrected compression ($\Delta h/h_0$) of the sample as is shown in figure 2 from diagram no. 9 on. Of special interest is the influence of the dissipated mechanical energy within the specimen which will be a balance of heat production and heat loss as was pointed out in section 2. Therefore, the area of the corrected function $F(\Delta h)$ in diagram no. 9 will be divided into small elements as it has been done also for the mechanical corrections in the diagrams no. 3

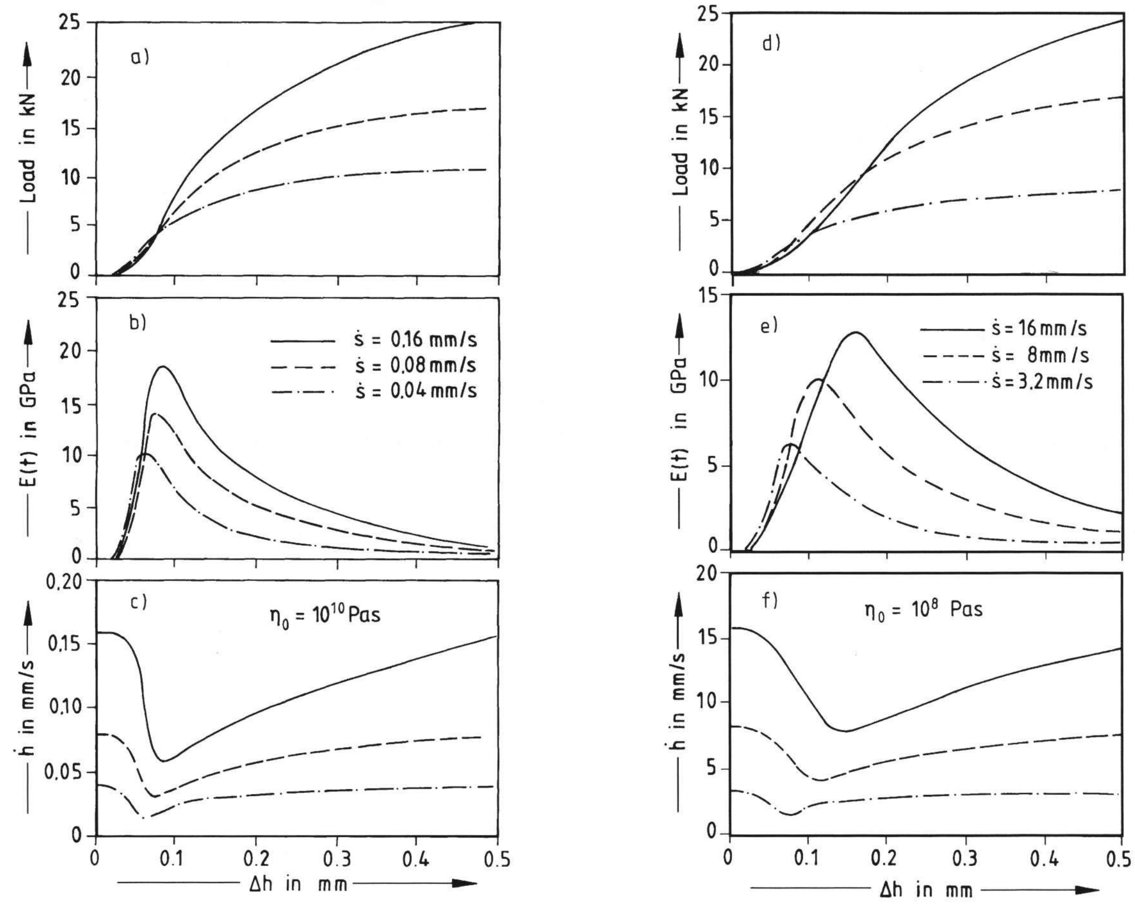

Figures 8a to f. Load, F (figures a and d), relaxation modulus, $E(t)$ (figures b and e), and axial deformation rate, $\dot{h}$ (figures c and f), versus axial deformation, Δh, at two Newtonian viscosities, $\eta_0 = 10^{10}$ and 10^8 Pa s, and three piston velocities: $\dot{s} = 0.16$, 0.08 and 0.04 mm/s at $\eta_0 = 10^{10}$ Pa s and $s = 16$, 8 and 3.2 mm/s at $\eta_0 = 10^8$ Pa s.

to 10 in figure 2 in order to regard first the whole mechanical energy which is put into the sample under adiabatic condition according to equation (4) and figure 11:

$$\begin{aligned} \mathrm{d}Q_i^{\mathrm{in}} &= \frac{1}{2}(F_i + F_{i-1})(\Delta h_i - \Delta h_{i-1}) = \\ &= \frac{1}{2}(F_i + F_{i-1})\,\mathrm{d}\Delta h_i \end{aligned} \tag{15}$$

where F_i is the load and $\mathrm{d}\Delta h_i$ is the deformation increment.

The heat loss is treated similarly stepwise as in equation (15) according to equation (5):

$$\mathrm{d}Q_i^{\mathrm{out}} = (\alpha_{\mathrm{cd}}\, 2A_{\mathrm{cd}} + \alpha_{\mathrm{r}} A_{\mathrm{r}} + \alpha_{\mathrm{cv}} A_{\mathrm{r}})\, \Delta T_{i-1}^{\mathrm{net}}\, \mathrm{d}\Delta h_i / \dot{h}_i \tag{16}$$

with $\mathrm{d}\Delta h/\dot{h} = \mathrm{d}t$ the infinitesimal time interval and $\Delta T_{i-1}^{\mathrm{net}}$ the net temperature increase during the deformation Δh_{i-1}.

The summation of the difference of equations (15 and 16) leads to the total net temperature increase ΔT^{net} during the compression process of the sample. Introducing equations (15 and 16) into equation (6) gives:

$$\begin{aligned} \mathrm{d}\Delta T_i^{\mathrm{net}} = \frac{1}{c_{\mathrm{p}} M} \Bigg[& \frac{F_i + F_{i-1}}{2}\, \mathrm{d}\Delta h_i - \\ & - (\alpha_{\mathrm{cd}} A_{\mathrm{cd}} + \alpha_{\mathrm{r}} A_{\mathrm{r}} + \alpha_{\mathrm{cv}} A_{\mathrm{r}})\, \Delta T_{i-1}^{\mathrm{net}}\, \mathrm{d}\Delta h_i / \dot{h} \Bigg] \end{aligned} \tag{17}$$

where c_{p} can be determined by the equation of Moore and Sharp [15]. A concrete calculation formula of $\mathrm{d}Q_i^{\mathrm{out}}$ and $\mathrm{d}T_i^{\mathrm{net}}$ is given in section 7.

The total net temperature increase corresponding to the deformation Δh_i is:

$$\Delta T_i^{\mathrm{net}} = \sum \mathrm{d}\Delta T_i^{\mathrm{net}}\,. \tag{18}$$

The adiabatic temperature increase corresponding to Δh_i is:

$$\Delta T_i^{\max} = \sum \mathrm{d}\Delta T_i^{\max} = \sum \frac{F_i + F_{i-1}}{2 c_{\mathrm{p}} M}\, \mathrm{d}\Delta h_i\,. \tag{19}$$

This thermal procedure is introduced into the computer programme of the mechanical procedure. The whole programme may plot not only the main properties resulting from the experiments but also detailed results at

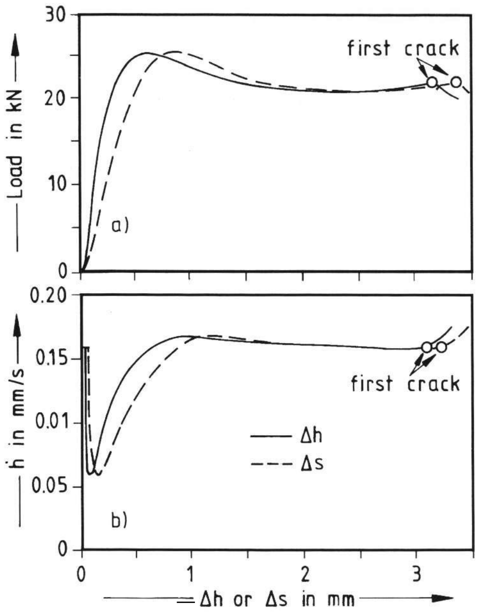

Figures 9a and b. Load, F (figure a), and deformation rate, $\dot{h}$, of the sample (figure b) versus deformation, Δh, of the sample and piston movement, Δs, respectively, at a Newtonian viscosity $\eta_0 = 10^{10}$ Pa s and at a piston velocity of $\dot{s} = 0.16$ mm/s, ——: versus Δh, – – –: versus Δs.

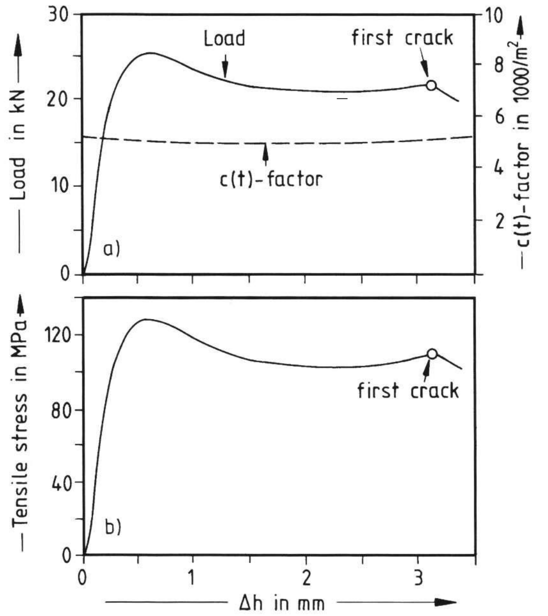

Figures 10a and b. Load, F, and tensile stress factor, $c(t)$ (figure a), and tensile stress (figure b) versus axial deformation, Δh, at $\eta_0 = 10^{10}$ Pa s and at $\dot{s} = 0.16$ mm/s.

any step of the programme with and without regard to certain parameters of special interest in order to study the various influences of these parameters on the desired properties as a function of stress, deformation rate, degree of compression etc. These influences will be studied and guided here by characteristic examples.

Figures 12a and b show the temperature increase produced by the mechanical deformation energy during compression versus sample deformation at two different

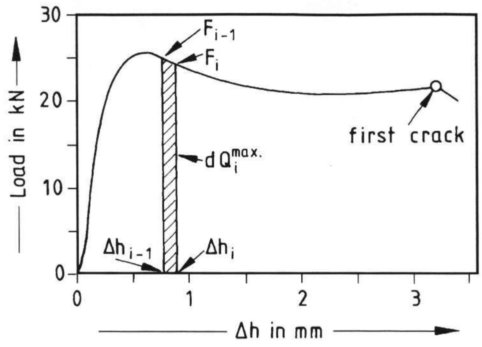

Figure 11. Typical load-deformation diagram of a compressed cylindrical glass sample at $\eta_0 = 10^{10}$ Pa s and a piston velocity $\dot{s} = 0.16$ mm/s with infinitesimally dissipated maximum heat $dQ_i^{\max}$ from mechanical energy $\frac{1}{2}(F_{i-1} + F_i)(\Delta h_i - \Delta h_{i-1})$.

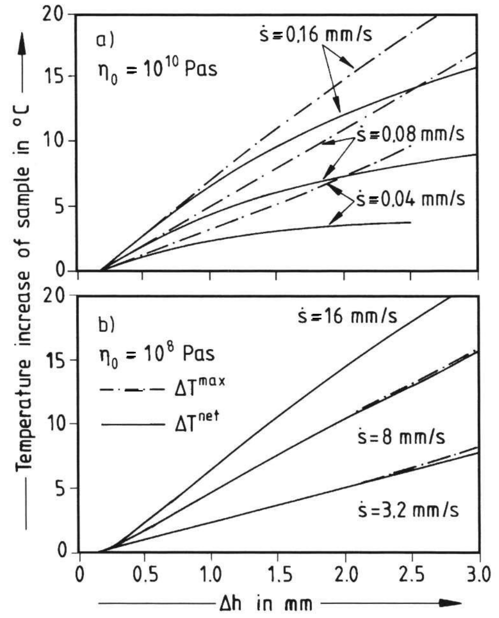

Figures 12a and b. Temperature increase, $\Delta T^{\max}$ and ΔT^{net}, produced by the mechanical energy during compression versus axial deformation of the sample, Δh, at two Newtonian viscosities $\eta_0 = 10^{10}$ and 10^8 Pa s and six piston velocities. $\Delta T^{\max}$ (–·–·–): adiabatically dissipated energy without heat loss; ΔT^{net} (——): with heat loss from sample to the surrounding.

(Newtonian) equilibrium viscosities and at three piston velocities for the maximum (adiabatic) temperature increase, $\Delta T^{\max}$ (dashed curves), calculated with equation (4) and for the net temperature increase, ΔT^{net}, (solid curve) according to equation (6). It is seen from these plots that the difference between $\Delta T^{\max}$ and ΔT^{net} becomes smaller with increasing deformation rate and even disappears at the equilibrium viscosity $\eta_0 = 10^8$ Pa s (figure 12b). This means that the compression process at viscosities $\eta_0 < 10^8$ Pa s can be regarded as an adiabatic one because the deformation rate is so high that the heat production rate, dQ_{in}/dt, becomes much larger than the heat loss rate, dQ_{out}/dt (see equation (8) in section 2.). The consequences for the viscosity decrease (see equation (7)) are shown in the following figures.

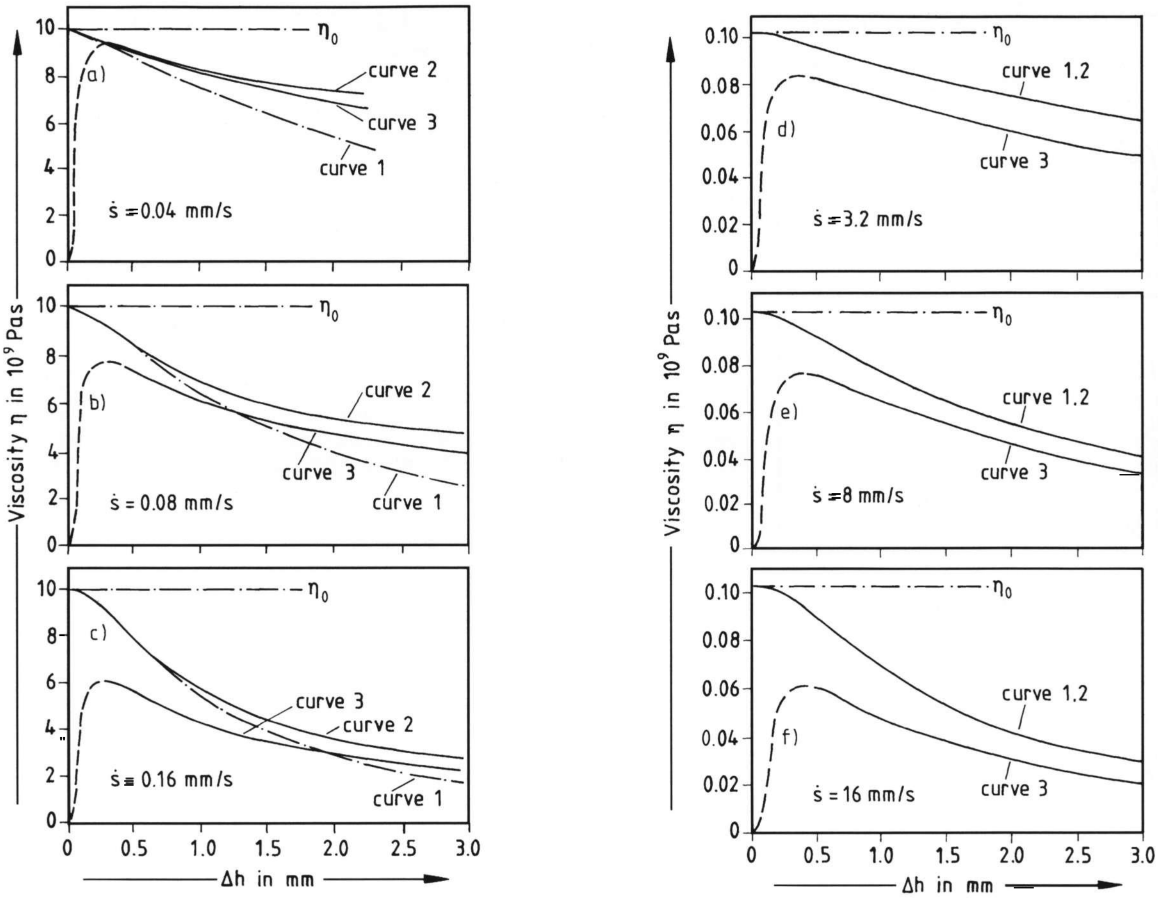

Figures 13a to f. Viscosity versus axial compressive deformation, Δh, at various piston velocities and at two Newtonian viscosities, $\eta_0 = 10^{10}$ Pa s (figures a to c) and at $\eta_0 = 10^8$ Pa s (figures d to f). Curves 1: viscosity decrease with the assumption that the total mechanical energy is dissipated; curves 2: viscosity decrease with consideration of heat loss during deformation; curves 3: viscosity decrease obtained experimentally from the load-deformation diagram directly and application of the Gent equation only without thermal corrections.

Figures 13a to f represent the viscosity versus the real axial compressive deformation of the sample at different equilibrium viscosities, $\eta_0 = 10^{10}$ Pa s (figures a to c), $\eta_0 = 10^8$ Pa s (dot-dashed lines; figures d to f). Curves 1 show the decrease of the viscosity, $\eta_{0T}(\Delta T^{\max}) = \eta_{0T_{\max}}$, calculated with the assumption that the total mechanical energy is adiabatically dissipated ($\Delta T^{\mathrm{net}} = \Delta T^{\max}$ in equation (6)). Curves 2 are correlated to ΔT^{net} (subtraction of heat loss) and respectively to $\eta_{0T}(\Delta T^{\mathrm{net}}) = \eta_{0T_{\mathrm{net}}}$. Curves 3 represent the decrease of viscosity $\eta = \eta(t)$ as determined from the experimental load-deformation diagram and from the Gent equation (3) without any temperature correction. It is remarkable that the curves 1 and 2 coincide in figures 13d to f at the given piston velocities because the compression processes turn to the adiabatic ones at such large deformation rates.

The ratio $\eta/\eta_{0T_{\mathrm{net}}}$, the normalized non-Newtonian viscosity, describes the realistic and pure non-Newtonian flow behaviour over the whole deformation range as is shown by the solid curves in figures 14a and b. At larger deformations the ratio deviates systematically with increasing deformation, Δh, under the adiabatic considerations ($\eta/\eta_{0T_{\max}}$) at large (Newtonian) equilibrium viscosities, η_0, (see dot-dashed curves in figure 14a). This deviation disappears at equilibrium viscosities of $\eta_0 = 10^8$ Pa s (figure 14b) for the same reason as was mentioned about the curves 1 and 2 in figures 13d to f because the compression process becomes adiabatic. It has to be pointed out that the increasing part of all the curves in figures 13a to f and 14a and b within the range from zero to the maximum values are unrealistic but from there on they are realistic.

In order to investigate the influence of ΔT^{net} on the values of the applied stress on the samples, the axial stress under non-Newtonian flow, σ_c, was caculated with the assumption that there is no thermally induced viscosity decrease caused by mechanical energy dissipation during the compression process:

$$\sigma_c(t) = \sigma_{ax} + m(\eta_0 - \eta_{0T_{\mathrm{net}}})\,\dot{\varepsilon}(t) \qquad (20)$$

where σ_{ax} is the measured axial stress (which is lower than σ_c due to the temperature influence), η_0 the (Newtonian) equilibrium viscosity, $\dot{\varepsilon}(t) = \dot{h}(t)/h(t)$ the normalized deformation rate, m depends on boundary condition, with slip or without slip between the glass sample and the pistons; $m = 3$ for slip or tensile stress, $m = 3\,(1 + R^2/(2\,h(t)^2))$ for no slip after Gent and Nadai

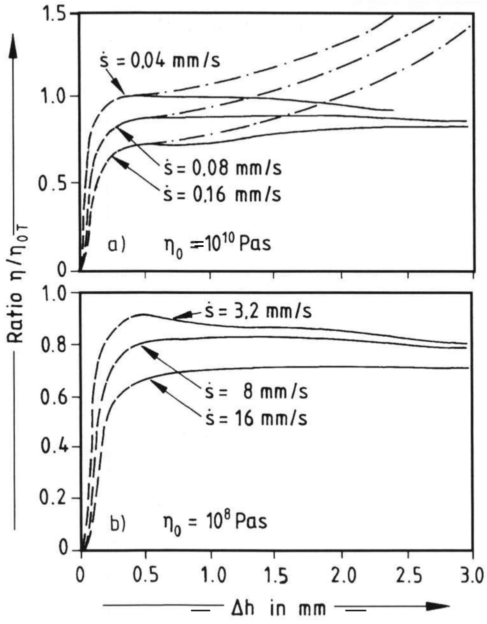

Figures 14a and b. Normalized non-Newtonian viscosity, η/η_{0T}, versus axial deformation, Δh, at two Newtonian viscosities, $\eta_0 = 10^{10}$ Pa s (figure a) and 10^8 Pa s (figure b) and various piston velocities. ——: with heat loss (Q_{net}), —·—·—: without heat loss (Q_{in}).

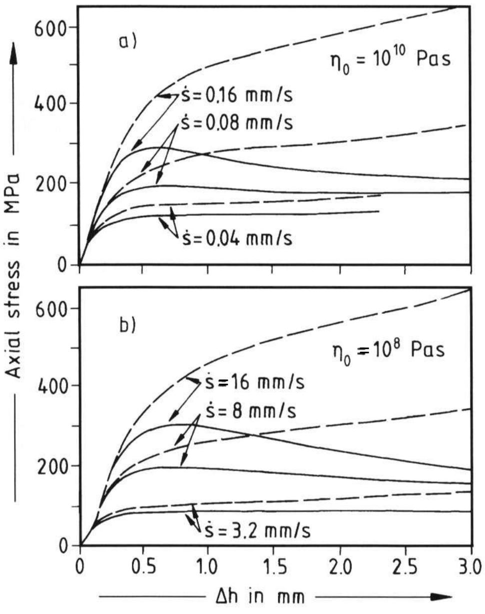

Figures 15a and b. Axial compressive stresses versus sample deformation, Δh, at various piston velocities, $\dot{s}$, and at different Newtonian viscosities $\eta_0 = 10^{10}$ (figure a) and 10^8 Pa s (figure b). ——: σ_{ax} calculated from the experimental load-deformation diagram; – – –: σ_{c} corrected with equation (20).

which is explicitely demonstrated in [16]. σ_{c} and σ_{ax} are represented by the dashed and solid curves, respectively, in figures 15a and b. It is clearly seen that the dissipated mechanical energy within the sample has drastically reduced the axial stress, σ_{ax}, particularly at larger deformation rates.

If equation (20) is introduced into the Gent equation (3) the net non-Newtonian viscosity $\eta_{\text{nN}}(t)$ (solid curves in figures 16a and b) is obtained, i.e. the viscosity which is corrected by the net temperature increase, ΔT_{net}:

$$\eta_{\text{nN}}(t) = \frac{A_{\max}[\sigma_{\text{ax}}(t) + m(\eta_0 - \eta_{0T_{\text{net}}})\dot{h}(t)/h(t)]}{3\,V\dot{h}[V/(2\pi h(t)^5) + 1/h(t)^2]} \tag{21}$$

where $A_{\max} = \pi r_{\max}^2 = \pi R^2 (h_0/h(t))^p$ and p depends on the boundary condition between glass sample and piston (see equation (23) and figures 17a and b). Again the dashed initial part of the curves in figures 16a and b is unrealistic up to the maximum.

The non-Newtonian viscosity, η_{nN}, can also be written as:

$$\eta_{\text{nN}} = \eta(t) + (\eta_0 - \eta_{0T_{\text{net}}}) \tag{22}$$

where $\eta(t)$ is the as-measured viscosity after the Gent equation without correction of the thermal effect.

If η_{nN} is divided by η_0, η_{nN}/η_0, it may be called the normalized non-Newtonian viscosity which describes also the non-Newtonian flow behaviour of glass melts. This would give similar curves as those in figures 16a and b. In earlier papers [10 to 12] the ratio $\eta(t)/\eta_{0T_{\max}}$ was given, where $\eta_{0T_{\max}}$ is the $\Delta T_{\max}$-corrected viscosity after equation (7) at small degrees of deformation ($\Delta h/h_0 \le 4\,\%$). $\eta_{0T_{\text{net}}}$ of the ratio $\eta(t)/\eta_{0T_{\text{net}}}$ in the present paper is the ΔT_{net}-corrected viscosity after equation (7). The only difference between $\eta(t)/\eta_{0T\text{net}}$ and η_{nN}/η_0 is that the ΔT_{net} correction in the former ratio is made with respect to $\eta_{0T\text{net}}$ and in the latter ratio with respect to η_{nN} directly (equation (21)) and both are equivalent to each other. In contrast to this the $\Delta T_{\max}$-corrected viscosity is valid only at large $\dot{h}$ values, which correspond to high temperatures for a given amount of σ_{ax}.

The boundary condition between the glass samples and the piston has been studied intensively. In figures 17a and b are plotted the maximum diameters at the equatorial line versus the decreasing height $h(t)$ of the compressed cylindrical glass samples at different viscosities and for totally different glass compositions, calculated theoretically in [16] under slip ($m = 3$) and no slip condition ($m = 3(1 + R^2/2\,h(t)^2)$) as compared with experimentally determined values. The change of these maximum radius, $r_{\max}$, is represented by the following relations:

without slip [11]: $r_{\max} = R(h_0/h(t))^{0.75}$; (23)

with slip: $r_{\max} = R(h_0/h(t))^{0.5}$; (24)

experimental: $r_{\max} = R(h_0/h(t))^{0.57}$. (25)

The experimental values show a good fit by equations (23 to 25) independent of the type of glass (silicate glasses) and independent of viscosity and deformation

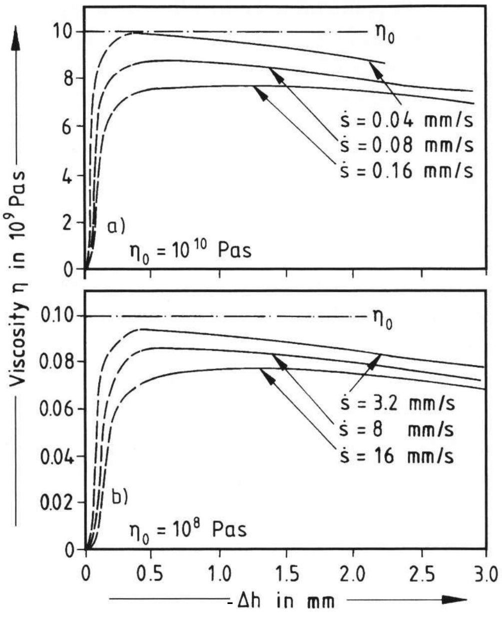

Figures 16a and b. Non-Newtonian viscosity, η_{nN}, calculated and temperature-corrected with equation (20), versus axial compressive deformation, Δh, at various piston velocities and at two Newtonian equilibrium viscosities $\eta_0 = 10^{10}$ (figure a) and 10^8 Pa s (figure b).

rate, $\dot{s}$. Therefore, equation (25) is used for the calculation of the stress from the measured force, F. At small deformation values it is $r_{\max} \approx R$ (see also section 3.3. and figures 18a to h).

3.3. Rheological influences on the numerical treatment of the cylinder compression experiment

The rheology of the compression experiment is influenced by the following phenomena additionally to those described in sections 3.1. and 3.2.:

a) limits of the Nadai equations with respect to the degree and symmetry of the cylinder compression,

b) temperature distribution (gradient) produced by the heating equipment,

c) temperature and viscosity distribution produced by inhomogeneously dissipated mechanical friction energy,

d) non-Newtonian viscosity distribution.

To a): In order to prove this influence a series of compression experiments has been made to compare the geometry of the compressed glass cylinders with the geometry calculated from the Nadai equation. The experiments were made with float glass at a viscosity of 10^{10} Pa s (onset of non-Newtonian viscosity is about 140 MPa at 10^{10} Pa s [10]). In order to prove the influence of the non-Newtonian viscosity on the cylinder geometry, two different series were performed:

series 1 (samples 1 to 4, figures 18a to d and sample 1, figure 18e): $\dot{s}$ = 20 µm/s = constant, σ_{ax} = 70 MPa < σ_{initial}, $\Delta h/h_0$ ranging from 6.5 to 43 % of the original sample height;

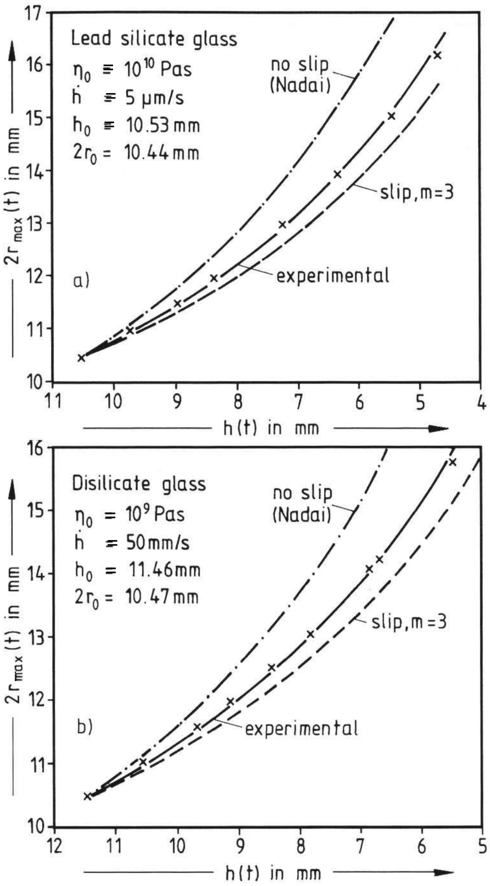

Figures 17a and b. Maximum diameter of compressed cylindrical glass samples at the equator line versus decreasing height, $h(t)$, for various boundary conditions between glass samples and pistons (see equations (23 to 25)); a) lead silicate glass at $\eta_0 = 10^{10}$ Pa s, b) disilicate glass at $\eta_0 = 10^9$ Pa s.

series 2 (samples 5 to 8, figures 18e to h): $\Delta h/h_0$ = = constant ≈ 40 %, $\dot{s}$ variable = 20, 40, 60, 80 µm/s and σ_{ax} variable = 70 to 210 MPa.

The compressed cylinders were photographed and enlarged, the theoretical geometries calculated by [11]:

$$r(t) = R\exp\left[-0.75\left(\ln h(t) + \frac{z^2}{2h^2(t)} - \ln h_0 - \frac{z^2}{2h_0^2}\right)\right]$$
$$= R(h_0/h(t))^{0.75}\exp\left[\frac{3}{8}\left(z^2/h_0^2 - z^2/h(t)^2\right)\right] \quad (26)$$

where R is the original radius of the cylinder, h_0 the original height, $r(t)$ the variable radius at time t as a function of z, $h(t)$ the height at time t, and z the current variable in the cylinder axis. The obtained results are: first, the two series show a relatively good agreement between the theoretical and experimental cylinder geometries. The largest deviations (≈ 7 to 8 %) are in the equator range (figures 18e to h) at compression degrees of $\Delta h/h_0$ = 30 %. Therefore, only compression values of maximum $\Delta h/h_0$ = 30 to 40 % are applied as was also done with former measurements, however, only for tensile strength measurements

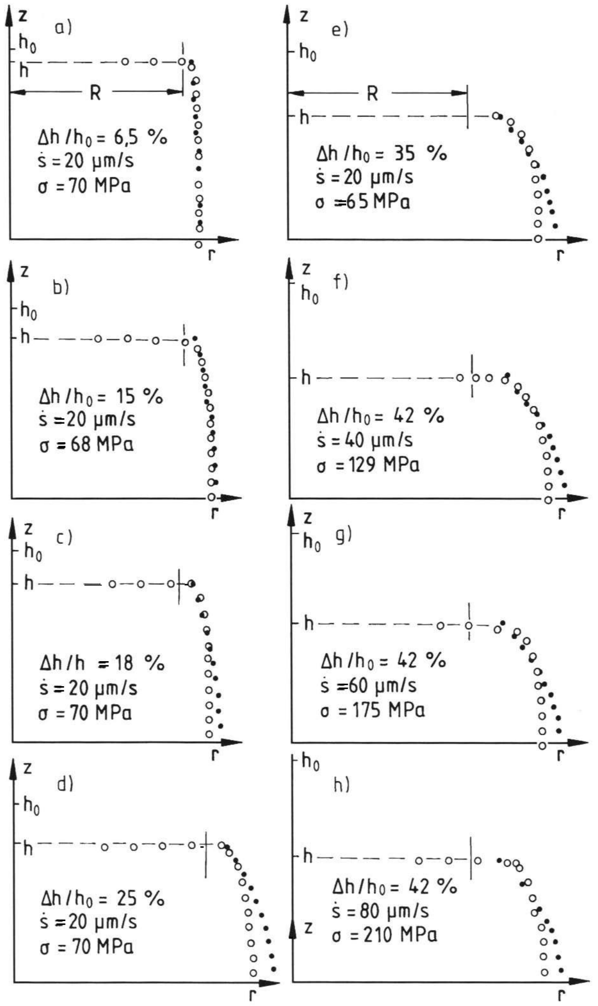

Figures 18a to h. Comparison between experimentally determined (○○○) and theoretically calculated (●●●, after Nadai) geometries of glass cylinders compressed in different manner; a) to d) $\dot{s}$ = 20 µm/s = constant, σ_{ax} = 70 MPa = constant < < σ_{initial}, $\Delta h/h_0$ = variable = 6.5 to 25 % at $\eta_0 = 10^{10}$ Pa s (σ_{initial} is the stress at which non-Newtonian flow occurs), e) to h) $\dot{s}$ = = variable = 20, 40, 60 and 80 µm/s, σ_{ax} = variable = 65 to 210 MPa > σ_{initial}, $\Delta h/h_0$ = constant ≈ 42 % at $\eta_0 = 10^{10}$ Pa s.

at large Δh values [10 to 12]. Second, no influence of the non-Newtonian viscosity on the sample geometry could be detected (figures 18a to h), because all samples which were compressed up to about 30 % show the same deviations of the radius at the equator line of 7 to 8 %. Third, from the enlarged photos of the cylinder geometry at the transition range cylinder face area/cylinder surface is observed a roundness which points out that one can proceed on the assumption of adhesion at the cylinder face areas because in this region is $r_{\text{Nadai}} > r_{\text{experim}}$, where the Nadai equation is also an approximation. If, however, instead of equation (23) equation (25) is applied (and/or equation (26) but with the exponent 0.57 instead of 0.75) the deviations from the discussed experimental geometry in figures 18a to h will be vanished. These figures show also that the change of geometry is independent of the composition of glasses, η_0 and $\dot{s}$.

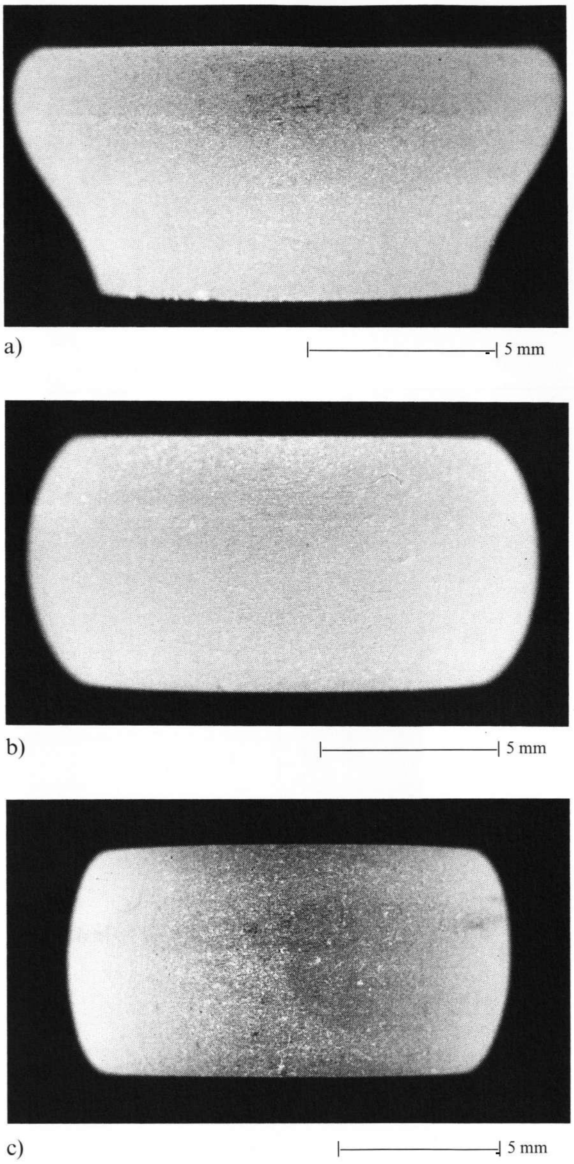

Figures 19a to c. Influence of inhomogeneous and homogeneous temperature distribution on the geometric profile of compressed glass cylinders; a) temperature of the upper piston and the furnace temperature are about 50 K higher than that of the lower piston, b) temperatures of both pistons are about 50 K lower than the furnace temperature, c) homogeneous temperature distribution.

To b): The homogeneity of the temperature-constant zone of the furnace includes not only the atmosphere around the glass sample but also that of the two pistons [9]. Therefore, the pistons contain separated heating elements which have to be regulated together with the furnace in such a way that the temperature within the whole glass cylinder is satisfactorily constant. Figures 19a and b show examples of wrong temperature distribution, in figure 19a the lower piston has had an

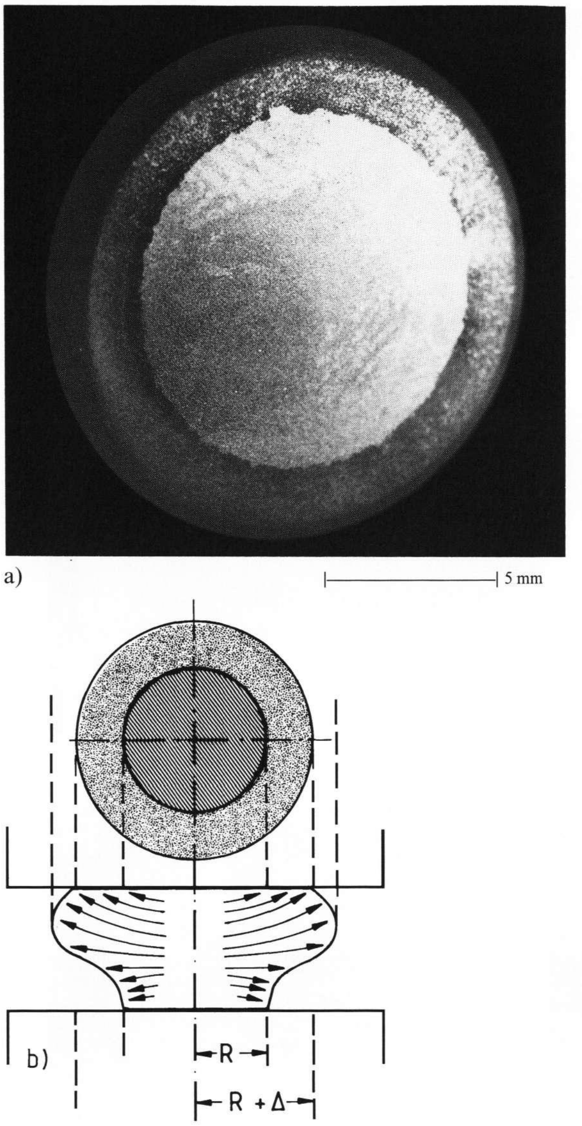

Figures 20a and b. View on the upper face area of the compressed glass cylinder of figure 19a showing no indication of slip although the radius, $R+\Delta$, seems to be much larger than the inital one. The initial radius R is seen clearly together with an outer ring having another surface reflectance than the inner circle area (figure a). The schematic view (figure b) illustrates how the enlargement of the upper face area may be accomplished by asymmetric flow without slip at the interface piston/glass melt.

about 50 K lower temperature than the upper one and the furnace, in figure 19b both pistons have had an about 50 K lower temperature than the furnace indicated by the larger curvature of the cylinder surface at the equator line compared with the sample of figure 19c which was compressed in a homogeneous temperature field including the temperature of the pistons. Figure 19a looks as if the sample has flowed by slip at the upper (hotter) piston. However, this is not true because from figure 20a one can see the original diameter of the glass cylinder without any flow by slip and the ring around this diameter which is produced by overlapping flow from inner layers of the cylinder to the hotter piston due to the compressive stress as is shown by figure 20b schematically.

To c): The flow lines within a compressed viscous glass cylinder are distributed in a complicated manner and viscous friction is largest in the middle of the cylinder and towards the equator line resulting in a local increase of temperature and a local decrease of viscosity. This kind of distribution is not regarded in these investigations but the effect is considered to be small as compared to the heat balance of section 3.2., particularly for small Δh values.

To d): Similar to point c) it is possible that along those flow lines with high viscous friction due to high shear rates a larger reduction of viscosity is obtained due to non-Newtonian flow behaviour than along flow lines with lower viscous friction. This leads together with c) to rheological inhomogeneities within the compressed glass samples. Strictly seeing, η_{nN} becomes a tensor because it becomes dependent on the distribution of the stresses, $\sigma(r, z)$, and deformation rates, $\dot{h}(r, z)$. But with respect to point a) as long as no influence of σ or $\dot{h}$ on the geometry of the compressed glass cylinder within 30 % deformation is observed, the assumption that η and η_{nN} are scalar quantities can be maintained as a good approximation. Therefore, the measured non-Newtonian viscosity for a certain deformation rate and stress, respectively, is a mean value over the whole glass cylinder. But this mean value gives enough information about the flow behaviour of glass melts with different structural arrangements.

4. Discussion and conclusions

The given analysis of the cylinder compression method for high-viscous glass melts is restricted to mathematical solutions in a closed manner. This has the great advantage that connections between the various parameters and variables can be presented in a clear arrangement as compared to solution methods for which algorithm procedures are applied, e.g. the method of finite elements, which was used successfully by Sakoske et al. [17].

As was shown in the first part, the most important problem is the limited stiffness of the experimental equipment, particularly at elevated temperatures. This requires the introduction of the experimentally determined correction function, called the system deformation, *SD*, (figure 2, diagrams no. 4 and 5 and figure 4, equation (1)), and the system deformation rate, $S\dot{D}$, which are experimentally determined in a successive way and which are closely connected to the load-deformation diagram of the glass sample (figure 2, diagrams no. 4 and 5, see also figures 4, 5b and c). In this way the real load-deformation curve, $F(\Delta h)$, of the sample itself is obtained free from the influence of the apparatus, from which the relaxation modulus, the Newtonian and non-Newtonian viscosity and the high-temperature tensile strength can be determined if the thermal influence can be neglected (at very small deformations) or if it is calculated (for large deformations).

So far, the thermal effect of dissipation of mechanical energy was estimated by calculating the maximum temperature increase, ΔT^{max}, from the adiabatical conversion of the total mechanical work into heat [10]. In order to evaluate a more realistic and more exact heat belance and to obtain the real temperature increase of the sample a thermal balance between heat production and heat loss leads to a net temperature increase, ΔT^{net}. The difference between ΔT^{net} and ΔT^{max} has a large effect on the evaluation of η/η_{0T}, particular at high deformations and viscosities.

As a result, the real non-Newtonian flow behaviour can be reflected by the ratio $\eta(t)/\eta_{0T_{\mathrm{net}}}$ and $\eta_{\mathrm{nN}}/\eta_0$, respectively, not only at small deformations but also within the whole deformation range. From figures 14a and b and 16a and b it is seen that if the deformation rate is high enough to induce non-Newtonian flow, the viscosity decreases drastically from the Newtonian equilibrium viscosity, η_0, to the non-Newtonian viscosity, η_{nN}, within the small deformation range $\Delta h/h_0 = 3$ to 4 % and then it changes more slightly during further deformation up to $\Delta h/h_0 \approx 30\,\%$. The existence of the first step of viscosity decrease may be attributed to a significant structural rearrangement process within the glass melt which continues more slightly after that. This point is discussed in [2, 3, 9 and 10] and will be discussed on elsewhere. If glass melts with different chemical compositions are compared under this aspect it is important that the effect of non-Newtonian viscosity, relaxation modulus and high-temperature tensile strength should be measured not at the same temperature but at the same Newtonian viscosity, η_0, i.e. at isochomal conditions.

It is suggested in figures 15a and b that not only the non-Newtonian flow effect but also the heating effect plays an important part with respect to the decrease of applied stress. Due to this common influence this may be of special advantage in practise because the deformation rate $\dot{h}$ is sharply increased at a given axial stress and vice versa. These two effects may enhance workability of glass melts, particularly that of "short" glass melts since they have a larger viscosity-temperature gradient $\mathrm{d}\eta_0/\mathrm{d}T$. This conclusion may be of some interest for the forming of glass, e.g. for the press-and-blow process.

As is well known, the working range of bottle press-and-blow operation is usually between 10^5 and $\approx 10^7$ Pa s which corresponds to a forming rate range of 30 to $\approx$ 40 cm/s. According to the analysis in section 2., the compression process of container glasses can be considered as an adiabatic one at these viscosities, thus, as a result of the mechanical energy dissipation, the forming rate can be raised for a given load.

However, in the fiber drawing process, the heating effect can usually be neglected at normal drawing stresses and for thin fibres ($r < 20$ µm) since the heat loss rate at low drawing rates is larger due to the very large specific surface, but under extreme fibre drawing conditions the shear-thinning effect could be observed together with the heating up by the dissipation of the mechanical forming (drawing) energy [18].

The whole procedure of the cylinder compression method concerning the mechanical and thermal influences and parameters on the viscoelastic properties of glass melts as shown in this paper were treated by computer programmes which allow to give information not only on the mutual influence of the considered parameters in total but also on certain parameters separately in order to study their individual special effects.

*

These investigations were conducted with kind supports of the Deutsche Forschungsgemeinschaft (DFG), Bonn-Bad Godesberg, and of the Arbeitsgemeinschaft industrieller Forschungsvereinigungen (AiF), Köln, by agency of the Hüttentechnische Vereinigung der Deutschen Glasindustrie (HVG), Frankfurt/M., through the resources of the Bundesminister für Wirtschaft (BMWi), Bonn.

5. List of symbols

A	cross-section of the compressed glass sample
A, B, T_0	constants of the Vogel-Fulcher-Tamman equation
$A_{\mathrm{cd}}, A_{\mathrm{r}}, A_{\mathrm{cv}}$	areas corresponding to α_{cd}, α_{r} and α_{cv}
A_{max}	maximum cross-section of the compressed sample = equatorial cross-section
a, b	constants of the system deformation function in equation (1)
C_{s}	Stefan-Boltzmann radiation constant
c_{p}	specific heat of the glass sample
$c(t)$	tensile stress factor for the stress at the equatorial line of the compressed glass cylinder
$E(t)_{\mathrm{max}}$	relaxation modulus, $E(t)$ at PI of the force-Δh plot (or maximum of $E(t)$)
F	$= F(t) =$ compressive force as a function of time t or/and s
$\dot{F}$	$= \mathrm{d}F/\mathrm{d}t$
h_0	initial height of the glass cylinder
$h(t)$	cylinder height at time t
$\dot{h}(t)$	$= \mathrm{d}\Delta h/\mathrm{d}t = \lvert \mathrm{d}h/\mathrm{d}t \rvert$, i.e. deformation rate of the sample
h_{N}	$= h/2 =$ half of the cylinder height after Nadai
k	heat transmission coefficient
l_{s}	depth of conduction into the steel piston
M	mass of glass sample
m	factor for tensile experiment, slip and no slip condition
n	constant of system deformation function (equation (1))
Nu	Nusselt number
p	exponent for A_{max} depending on boundary condition between glass and piston
PI	index for point of inflexion

$\dot{Q}$	$= \mathrm{d}Q/\mathrm{d}t$, i.e. heat flow rate or rate of heat gain or loss
Q_{in}	maximum dissipated heat quantity produced within the glass sample under adiabatic condition
Q_{net}	net heat quantity, $Q_{\mathrm{in}} - Q_{\mathrm{out}}$
Q_{out}	heat loss of the cylindrical glass sample
R	initial radius of the glass cylinder
r, z	radial and axial cylinder coordinates
s	piston movement linearly proportional to time
$\dot{s}$	piston velocity
SD	system deformation
$\dot{SD}$	system deformation rate $= \mathrm{d}SD/\mathrm{d}t$
T	temperature
t	time
V	volume of glass sample
v_0	$= \dot{h}/2 \equiv$ axial deformation rate
α_{cd}	heat conduction coefficient of the glass sample
α_{cv}	heat convection coefficient of the glass sample
α_{f}	heat transfer coefficient from glass to steel piston
α_{r}	heat radiation coefficient of the glass sample
$\Delta h(t)$	$= h_0 - h(t)$, i.e. sample deformation at time t
$\Delta T^{\max}$	maximum temperature increase under adiabatic condition
ΔT^{net}	net temperature increase
ε_{G}	emission ratio of the glass sample
$\dot{\varepsilon}(t)$	$= \dot{h}(t)/h(t)$, i.e. normalized deformation rate
η	$= \eta(t)$, i.e. viscosity as measured and determined after Gent without ΔT correction
$\eta_{\mathrm{nN}}(t)$	non-Newtonian viscosity without thermally induced effects
η_0	Newtonian (equilibrium) viscosity
η_{0T}	Newtonian viscosity corrected by the temperature increase ($\Delta T^{\max}$ or ΔT^{net}) due to dissipated heat Q_{in} or Q_{net}
λ_{G}	thermal conductivity of the glass sample
λ_i	specific factor
λ_{L}	thermal conductivity of furnace atmosphere (air)
λ_{s}	thermal conductivity of the steel (pistons)
σ	axial stress
σ_{ax}	axial compressive stress as measured without thermal correction
σ_{c}	axial stress, thermally corrected
$\sigma_{\mathrm{r}}, \sigma_{\mathrm{t}}, \sigma_{\mathrm{z}}$	stress components within the compressed sample (r = radial, t = tangential, z = axial)
$\sigma(t)_{\mathrm{tensile}}$	tensile stress
$\sigma(t)_{\mathrm{tensile}}^{\max}$	tensile strength $\equiv$ stress at the first crack of the compressed glass cylinder

6. References

[1] Li, J. H.; Uhlmann, D. R.: The flow of glass at high stress levels. Pt. 1. Non-Newtonian behavior of homogeneous $0.08\,\mathrm{Rb_2O} \cdot 0.92\,\mathrm{SiO_2}$ glasses. J. Non-Cryst. Solids **3** (1970) p. 127–147.

[2] Simmons, J. H.; Mohr, R. K.; Montrose, C. J.: Non-Newtonian viscous flow in glass. J. Appl. Phys. **53** (1982) no. 6 p. 4075–4080.

[3] Simmons, J. H.; Ochoa, R.; Simmons, K. D. et al.: Non-Newtonian viscous flow in soda-lime-silica glass at forming and annealing temperatures. J. Non-Cryst. Solids **105** (1988) p. 313–322.

[4] Manns, P.; Brückner, R.: High temperature fracture (above T_g) and non-Newtonian flow behaviour of soda-lime-silicate glass in a parallel-plate-plastometer. In: Kurkjian, C. R. (ed.): Proc. NATO-Workshop on strength of inorganic glass. Algarve 1983. New York, London: Plenum Press 1985. p. 549–565.

[5] Webb, S. L.; Dingwell, D. B.: Onset of non-Newtonian rheology of silicate melts: a fibre elongation study. Phys. Chem. Minerals **17** (1990) p. 125–132.

[6] Gent, A. N.: Theory of the parallel plate viscometer. Br. J. Appl. Phys. **11** (1960) p. 85–88.

[7] Kent, R.; Rawson, H.: An experimental and theoretical investigation of glass pressing. Glass Technol. **12** (1971) no. 5, p. 117–127.

[8] Schumacher, R.: Thermische und mechanische Vorgänge beim Verpressen einer zähflüssigen Glasschmelze. Glastech. Ber. **47** (1974) no. 11, p. 239–250.

[9] Manns, P.; Brückner, R.: Non-Newtonian flow behaviour of a soda–lime silicate glass at high deformation rates. Glastech. Ber. **61** (1988) no. 2, p. 46–56.

[10] Hessenkemper, H.; Brückner, R.: Load-dependent flow behaviour of silicate glass melts. Glastech. Ber. **61** (1988) no. 11, p. 312–320.

[11] Hessenkemper, H.; Brückner, R.: Relaxation behaviour, high-temperature tensile strength and brittleness of glass melts. Glastech. Ber. **62** (1989) no. 12, p. 399–409.

[12] Hessenkemper, H.; Brückner, R.: Load-dependent relaxation behaviour of various glass melts with different structural configurations. Glastech. Ber. **63** (1990) no. 1, p. 1–6.

[13] Nadai, A. L.: Theory of flow and fracture of solids. New York: McGraw-Hill 1963. p. 352–356.

[14] Habeck, A.; Brückner, R.: Direct connection between anisotropic optical properties, polarizability and rheological behaviour of single-phase glass melts. J. Non-Cryst. Solids **162** (1993) p. 225–236.

[15] Moore, J.; Sharp, D. E.: Note on calculation of effect of temperature and composition on specific heat of glass. J. Am. Ceram. Soc. **41** (1958) no. 11, p. 461–463.

[16] Yue, Y.; Brückner, R.: A new description and interpretation of the flow behaviour of high-viscous glass melts. J. Non-Cryst. Solids. (In press.)

[17] Sakoske, G. E.; Rekhson, S. M.; Cooper, A. R.: Flow and fracture of glass cylinders pressed between parallel plates. In: XVI International Congress on Glass, Madrid 1992. Vol. 4. p. 9–14. (Bol. Soc. Esp. Ceram. Vid. **31-C** (1992) no. 4.)

[18] Brückner, R.; Pähler, G.; Stockhorst, H.: Heißbruchmechanismen im Grenzbereich des Glasfaserziehvorganges. Glastech. Ber. **54** (1981) no. 3, p. 65–73.

[19] Eckert, E.: Einführung in den Wärme- und Stoffaustausch. 2nd ed. Berlin (et al.): Springer 1959.

[20] Scholze, H.: Glas. Natur, Struktur und Eigenschaften. 3rd ed. Berlin (et al.): Springer 1980.

[21] McGraw, D. A.: Heat transfer at the glass-mold interface. Glastech. Ber. **46** (1973) 89–91.

[22] Gardon, R.: The emissivity of transparent materials. J. Am. Ceram. Soc. **39** (1956) no. 8, p. 278–287.

[23] Coenen, M.: Messungen und Berechnungen über den zeitlichen Temperaturverlauf an der Grenzzone Metall/Glasschmelze. In: Advances in Glass Technology. Tech. Papers VI International Congress on Glass, Washington 1962. New York: Plenum Press 1962. p. 93–102.

[24] Trier, W.: Glasschmelzöfen. Berlin (et al.): Springer 1984.

7. Appendix

The heat loss of a glass cylinder which is heated up to ΔT larger than the surrounded furnace atmosphere and the two piston ends due to the dissipated mechanical energy is given by equation (5). The various quantities were calculated in the following ways. The heat transfer coefficient α_{cd} is given by [19]:

$$\alpha_{\mathrm{cd}} = 2\lambda_{\mathrm{G}}/h(t) \tag{27}$$

where $\lambda_{\mathrm{G}} = 10^{-3}\,\Sigma\,\lambda_i \cdot p_i$ is the thermal conductivity of the glass which depends on temperature and composition [15 and 20], $h(t)$ is the cylinder height at time t, and λ_i the specific factors, p_i the concentrations in wt% of the oxide components. The temperature dependence may be calculated according to [20]. The relation (27) is part of the coefficient of heat transmission coefficient, k, in axial direction from the sample to the pistons:

$$1/k = h(t)/(2\lambda_{\mathrm{G}}) + 1/\alpha_{\mathrm{f}} + l_{\mathrm{s}}/\lambda_{\mathrm{s}} \tag{28}$$

where α_f is the heat transfer coefficient from the glass sample to the steel pistons, λ_s is the thermal conductivity of the steel and l_s the depth of conduction into the steel piston. The boundary zone for α_f is very thin after McGraw [21] and changes with time from $2.5 \cdot 10^{-5}$ to about $2.5 \cdot 10^{-3}$ cm and α_f decreases from 25000 to 2000 J/(m^2 s K). In the present case the boundary zone is indeed still smaller than $2.5 \cdot 10^{-3}$ cm because of the axial pressure on the sample. Therefore, the heat resistance $1/\alpha_f$ through this zone will be one order of magnitude smaller than that of the glass sample $1/\alpha_{cd} = h(t)/2\,\lambda_G$. Also the heat transfer resistance of the pistons can be neglected because $l_s/\lambda_s \ll h(t)/2\,\lambda_G$.

Now, the heat losses by radiation and convection in radial direction are regarded. The radiation heat flow per unit time, unit area and Kelvin is given by:

$$q = \varepsilon_G \cdot C_s((T + \Delta T^{\mathrm{net}})^4 - T^4)/(10^8 \cdot \Delta T^{\mathrm{net}}) \tag{29}$$

where C_s is the Stefan-Boltzmann radiation constant of the black body ($C_s = 5.67$ J/(m^2 s K^4)), T the furnace temperature, ΔT^{net} the net temperature increase due to dissipated energy and ε_G the emission ratio which is between $0.9 < \varepsilon_G < 1$ [19] because the surface of the sample is much smaller than that of the furnace. ε_G decreases with decreasing thickness and increasing temperature after Eckert [19] and Gardon [22]. For a thickness of 10 mm and for temperatures between 450 and 650 °C ε_G is between 0.8 and 0.9, therefore α_r in equation (5) becomes:

$$\alpha_r = \varepsilon_G \cdot C_s\,((T + \Delta T^{\mathrm{net}}_{i-1})^4 - T^4)/(10^8\,\Delta T^{\mathrm{net}}_{i-1}) \tag{30}$$

where $\Delta T^{\mathrm{net}}_{i-1}$ is the temperature increase within the deformation section Δh_{i-1}.
After Coenen [23] the radiation transfer between glass and piston can be neglected.

The convective heat loss may be obtained from the Nusselt number, Nu, [19 and 24]:

$$\alpha_{cv} = Nu \cdot \lambda_L/h(t) \tag{31}$$

where λ_L is the thermal conductivity of the furnace atmosphere (air usually). An estimation gives a value of smaller than 10 J/(m^2 s K), i.e. $\alpha_{cv} \ll \alpha_r$ and α_{cd}, thus α_{cv} can also be neglected.

Introducing equations (27 and 30) into equation (16) gives:

$$\mathrm{d}Q_i^{\mathrm{out}} = \frac{4\lambda_G A_{cd}\,\mathrm{d}\Delta h_i}{h(t)\cdot\dot{h}}\,\Delta T^{\mathrm{net}}_{i-1} + \frac{\varepsilon_G \cdot C_s \cdot A_r\,\mathrm{d}\Delta h_i}{\dot{h}\cdot 10^8} \cdot \cdot\,[(T + \Delta T^{\mathrm{net}}_{i-1})^4 - T^4] \tag{32}$$

with the areas:

$$A_{cd} = 2\,V/h(t)\,, \tag{33}$$

$$A_r = 2\sqrt{\pi\,V h(t)}\,. \tag{34}$$

From equations (15, 17, 28 and 32) follows for the net temperature increase:

$$\mathrm{d}\Delta T_i^{\mathrm{net}} = \frac{1}{c_p M}\left[\frac{k_i + k_{i-1}}{2}\,\mathrm{d}\Delta h_i - \frac{4\lambda_G A_{cd}\,\mathrm{d}\Delta h_i}{h(t)\cdot\dot{h}}\,\Delta T^{\mathrm{net}}_{i-1}\right] - - \frac{\varepsilon_G C_s A_r\,\mathrm{d}\Delta h_i}{\dot{h}\cdot 10^8}\,(T + \Delta T^{\mathrm{net}}_{i-1})^4 - T^4) \tag{35}$$

with $\Delta T^{\mathrm{net}}_{i-1} = \sum_{1}^{i-1} \mathrm{d}\Delta T^{\mathrm{net}}_{i-1}$ (36)

and $\Delta T_i^{\mathrm{net}} = \Delta T^{\mathrm{net}}_{i-1} + \mathrm{d}\Delta T_i^{\mathrm{net}}\,.$ (37)